

Rodent Wearable Ultrasound Interrogation System for Wireless Neural Recording

Joshua Kay

Electrical Engineering and Computer Sciences
University of California at Berkeley

Technical Report No. UCB/EECS-2017-27

<http://www2.eecs.berkeley.edu/Pubs/TechRpts/2017/EECS-2017-27.html>

May 4, 2017



Copyright © 2017, by the author(s).
All rights reserved.

Permission to make digital or hard copies of all or part of this work for personal or classroom use is granted without fee provided that copies are not made or distributed for profit or commercial advantage and that copies bear this notice and the full citation on the first page. To copy otherwise, to republish, to post on servers or to redistribute to lists, requires prior specific permission.

Acknowledgement

I would like to thank David Piech for his valuable collaboration throughout the design process, especially for his work designing and fabricating the piezoelectric transducer array and neural dust mote. In addition, I would like to thank both Professor Bernhard Boser and Professor Michel Maharbiz for their exceptional insight and extensive technical knowledge that guided me through this research.

Rodent Wearable Ultrasound Interrogation System for Wireless Neural Recording

by Joshua E. Kay

Submitted to the Department of Electrical Engineering and Computer Sciences, University of California at Berkeley, in partial satisfaction of the requirements for the degree of **Master of Science, Plan II.**

Approval for the Report and Comprehensive Examination:

Committee:



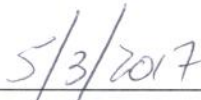
Professor Bernhard Boser
Research Advisor



Date



Professor Michel Maharbiz
Second Reader



Date

Abstract

Advancements in minimally-invasive, distributed biological interface nodes enable possibilities for networks of sensors and actuators to connect the brain with external devices. These brain machine interfacing systems require addressing three critical areas for real world use: signal-acquisition hardware, real-time operation, and long term validation. The recent development of the *neural dust* sensor mote has shown that utilizing ultrasound backscatter communication enables untethered sub-mm neural recording devices. These implanted sensor motes require a wearable external ultrasound interrogation device to enable *in-vivo*, unconstrained neural interface experiments. However, minimizing the complexity and size of the implanted sensors shifts the power and processing burden to the external interrogator. An ultrasound backscatter interrogator that supports real-time backscatter processing in a rodent-wearable, completely wireless device is presented. The device demonstrates a pulse-amplitude modulated non-return to zero level encoding which is intended for transmitting neural information. The ultrasound link is interfaced by a transducer array, which is driven by a 7-channel, high-voltage ultrasound interface ASIC. The system is controlled by a microcontroller which digitizes and processes the backscatter waveform and sends demodulated data to a remote client via bluetooth. This enables a compact ultrasound interrogation device intended for rodent neural interface experiments but applicable to other model systems. The wireless ultrasound interrogation device presented marks an integral step toward the development of practical brain machine interfacing technology.

Contents

1	Introduction	1
1.1	Motivation	1
1.2	Current State-of-the-art	2
1.3	Wireless Ultrasonic Backscatter Interrogation	3
1.4	Thesis Contribution	4
2	Ultrasonic Backscatter Interrogation Model	5
2.1	System Block Diagram	5
2.2	Losses in Tissues	6
2.2.1	The Material Transfer Function	7
2.2.2	The Material Impulse Response Function	8
2.3	Transducer Model	8
2.4	Scattering	9
2.5	Ultrasonic Communication Link Model	10
2.6	Simulation Results	11
2.7	Discussion	13
3	System Architecture	15
3.1	Requirements	15
3.2	System Overview	17
3.3	Electronics	18
3.4	Printed Circuit Board	19
3.4.1	Signal Integrity	19
3.4.2	Power Subsystem	20
3.5	Transducer	22
3.6	Wearable Device Software	24
3.7	Remote Client Software	27

4	Experimental Verification	30
4.1	Physical System	30
4.2	Experimental Setup	31
4.3	Results	32
4.3.1	Backscatter Signals	32
4.3.2	Neural Dust Mote Modulation Extraction	34
4.3.3	Bit Error Rate	35
4.4	Discussion	35
5	Conclusion	37
5.1	Future Work	37
5.2	Summary	38

List of Figures

2.1	System block diagram for ultrasonic backscatter interrogation system with implantable sensor as a series of frequency blocks	6
2.2	Schematic representation of KLM transducer model	9
2.3	Equivalent circuit for complete ultrasonic link model	11
2.4	Electrical excitation pulse	12
2.5	Received electrical backscatter signal with dust mote open and closed, respectively	12
2.6	Normalized backscatter peak amplitude versus neural modulation at $f = 1.8$ MHz	13
2.7	Comparison of simulated modulation depth (left) and measured modulation depth (right)	14
3.1	Mock system worn by rat	16
3.2	System Block Diagram	18
3.3	Simulation of power plane impedance vs. frequency	21
3.4	Simulated beam pattern of custom flex transducer with uniform phase across elements. Gray squares on the left and white overlaid squares on the right are transducer elements and the white box on the left is the dust mote position.	22
3.5	(Top left): Cross-section of ultrasound transducer stack-up. [a] flex PCB; [b] vias addressing each array element; [c] PZT active elements; [d] metalized PET layer; [e] absorptive backing layer of tungsten powder - filled polyurethane. (Top Right): flexible pcb prior to PZT bonding. (Bottom Left): Active elements after dicing. (Bottom Right): Finished transducer. All scale bars 2 mm.	23
3.6	Wearable device software flowchart	26
3.7	Remote client software flowchart	28
3.8	Graphical user interface on remote client	29

4.1	Physical design	31
4.2	Wearable interrogator seen by an adult male Long-Evans rat.	31
4.3	Experimental Setup	32
4.4	(Top) Received signal with dust mote open and closed, respectively. (Middle) Region of interest. (Bottom) Modulation depth.	33
4.5	Interrogation of “hello world” modulated on neural dust	34
4.6	Interrogated extracted value error	35

Chapter 1

Introduction

1.1 Motivation

Chronic monitoring of neural activity with minimally invasive medical devices creates broad opportunities from therapeutic treatments to human augmentation. Implanted sensors can achieve high spatio-temporal resolution but must overcome the inherent limitations of an invasive approach. Advances in minimally-invasive, distributed biological interface nodes promises to enable networks of sensors and actuators to interface between the brain and external devices. The realization of these networks may include prosthetics controlled by brain machine interfacing [1] or drug delivery systems [2]. These brain machine interfacing (BMI) systems consist of three key components: signal-acquisition hardware, feature extraction, and device output.

Despite recent achievements in BMI research and development, practical use of BMI systems require improvement in three critical areas: signal-acquisition hardware, real-time operation, and long term technology validation [3]. Practical signal-acquisition hardware systems must be convenient, portable, comfortable, and wireless. To achieve this, minimization of hardware size and power must be prioritized. Ideally, BMI systems seamlessly integrate into a user's ecosystem through a cosmetically acceptable device that is easy to setup and maintain. Additionally, the system should operate by telemetry to allow full mobility of the user. Fully invasive, implantable electrodes fall short of these requirements. Furthermore, invasive devices introduce challenges developing comfortable, convenient, and unobtrusive hardware, as invasive approaches require wires to pass directly through the skull. Brain machine interfacing hardware must extract neural signals in real-time to enable practical applications utilizing closed-loop neural modulation. Demonstrative

neural signal acquisition hardware [4] or systems design merely for neural recording [5] lack the real-time operation necessary for closed-loop neural modulation systems. Furthermore, clear validation of BMI systems’ efficiency, practicality, and impact on quality of life must be established before real-life deployment of the technology [6]. This requires long term study in *in-vivo* environments. Therefore, to realize practical BMI systems, wearable neural signal acquisition hardware must enable experimentation emulating real world use.

1.2 Current State-of-the-art

Current electrophysiological brain machine interface systems focus on either non-invasive or invasive signal acquisition approaches. Noninvasive approaches benefit from minimal risk and relative convenience; however, applications for noninvasive BMI systems have been limited to low-degree-of-freedom continuous movement controls and discrete selection. Scalp-recorded electroencephalographic activity was used for multidimensional point-to-point movement control using adaptive algorithms [7]. Motor imagery and associated oscillatory EEG signals from the sensorimotor cortex demonstrated control of a spelling device [8]. EEG signals reordered over sensorimotor areas enabled 2D control of a simple robotic arm [9]. Despite these achievements with noninvasive BMI, the applications are often limited to binary selection [10], [11], [12] or 2-dimensional control [13]. This is because common noninvasive approaches are limited to lower-frequency activity (less than 40 Hz). In contrast, invasive approaches, such as ECoG, offer superior spatial resolution and spectral bandwidth compared to noninvasive techniques, resulting in more sophisticated applications. ECoG includes higher-frequency activity (gamma band) up to 200 Hz. This higher frequency neural activity is highly correlated with motor, language, and cognitive function [14] [15]. ECoG systems have been used to decode sophisticated motor signals, such as finger [16], hand [17], and arm [18] movements. Intracortical microelectrode arrays provide another method of invasive neural recording. Using this technique, an implanted patient was able to learn to control a computer cursor during a 4-year trial [19]. In addition to inherent risks involved with invasive neural procedure, longevity of the invasive approaches will be a major hurdle toward practical deployment of this technology in the real world [20].

Each approach to neural interfacing provides it’s own advantages and disadvantages. While noninvasive approaches provide easy and safe methods for neural recording, the technology’s use of lower frequencies and insufficient spatial resolution limit the method’s effectiveness. On the contrary, invasive approaches have proven adequate to detect gamma band neural activity used to decode vital human functions,

but the need for trans-cranial wires and complicated surgical procedures creates longevity issues and adoption barriers. A compromise between these two approaches uses wireless implantable sensors to eliminate the need for trans-cranial wires while maintaining adequate resolution [21]. More recently, ultrasound has been demonstrated as a more efficient alternative to electromagnetic (EM) energy for wirelessly communicating and powering sub-mm implantable devices, as EM coupling becomes extremely inefficient in systems smaller than 5 mm due to inefficiency of coupling radio waves within tissue [22]. An ultrasonic backscatter interrogation system called neural dust demonstrated these advantages for sub-mm scale implantable devices used for wireless electrophysiological neural recording [1].

1.3 Wireless Ultrasonic Backscatter Interrogation

The neural dust technology is an ultrasonic backscatter system that demonstrates the advantages of ultrasound over electromagnetic (EM) coupling for sub-mm scale implantable devices used for wireless electrophysiological neural recording [1], [23], [24], [25]. Pulse-amplitude modulated passive backscatter communication, originally developed for radio-frequency identification technology [26], uses an external interrogator to send pulses of energy to backscatter devices. Impedance modulation of the backscatter device encodes information on the reflected wave, which is then decoded by the interrogator. This approach permits the backscatter node to be extremely low power, small, and simple, and is used when the constraints on the two sides of a wireless link are asymmetric. Backscatter communication links utilizing ultrasound have been explored in proof-of-principle experimental systems [27], [28] but lack the necessary integration for untethered *in-vivo* experimentation.

Minimizing the complexity and size of the implanted sensors shifts the power and processing burden to the external ultrasound interrogator. Prior work towards portable ultrasound systems suffer from high power consumption, requiring large capacity batteries or external power supplies [29]. This results in untethered systems that are too large and heavy to be worn [30] or wearable systems that are tethered to an external supply [31].

Moreover, the large amount of raw data in ultrasound systems imposes limitations on wireless transmission [32]. For example, the data rate in an ultrasound interrogation system with a single receive channel, 1000 16-bit samples per backscatter pulse, and a 5 kHz interrogation rate is 80 Mbps. This exceeds the 25 Mbps data rate limit of Bluetooth 4.0 and approaches the 250 Mbps data rate limit of the higher power WiFi Direct wireless option. The limited wireless options for ultrasound systems effectively tethers the ultrasound probe to a large central unit before processing can

be applied [33], resulting in large, high power devices. Various techniques may be applied on chip to reduce the data rate of ultrasound systems, such as backscatter peak detection for range estimation [34]. However, for ultrasonic backscatter interrogation systems, evolving implantable technologies benefit from flexible digital signal processing (DSP) capabilities.

1.4 Thesis Contribution

An ultrasound backscatter interrogator that supports real-time backscatter processing in a wearable, completely wireless device is presented. To overcome the power limitations of wearable ultrasound devices, the system's transducer drive-receive front end is a custom, 1.8 V supply high efficiency ASIC [35]. On board DSP techniques significantly reduce the data throughput of the ultrasound system, allowing for low power wireless solutions such as Bluetooth. This system enables a highly compact ultrasound interrogation device intended for rodent experiments but applicable to other model systems. By providing a convenient, portable signal-acquisition device that supports real-time, rodent *in-vivo* experimentation, this device galvanizes practical brain machine interfacing systems for real world applications.

Chapter 2

Ultrasonic Backscatter Interrogation Model

2.1 System Block Diagram

The wearable ultrasound system uses pulse-echo ultrasonic backscatter interrogation to communicate with implantable sensors. To better understand the behavior, tradeoffs, and limitations of ultrasonic backscatter interrogation, the system is modeled in MATLAB (Mathworks, Natick, MA). The block diagram for the major signals and acoustic processes is shown in figure 2.1. Each block is further explained in subsequent sections. $V_i(f)$ describes the electrical pulse excitation, $G_T(f)$ and $G_R(f)$ describe the transducer response, $A_T(f)$ describes the forward absorption of the acoustic attenuation in tissue, $S_n(f)$ describes the reflection from the implantable sensor mote, $A_R(f)$ describes the backward absorption of the acoustic attenuation in tissue, and $V_o(f)$ describes the received electrical signal. This system can be summarized by the following equation in the frequency domain

$$V_o(f) = V_i(f)G_T(f)A_T(r, f)S_n(r, f)A_R(r, f)G_R(f) \quad (2.1)$$

or the time domain

$$v_o(t) = v_i(t) * g_T(t) * a_T(r, t) * s_n(r, t) * a_R(r, t) * g_R(t) \quad (2.2)$$

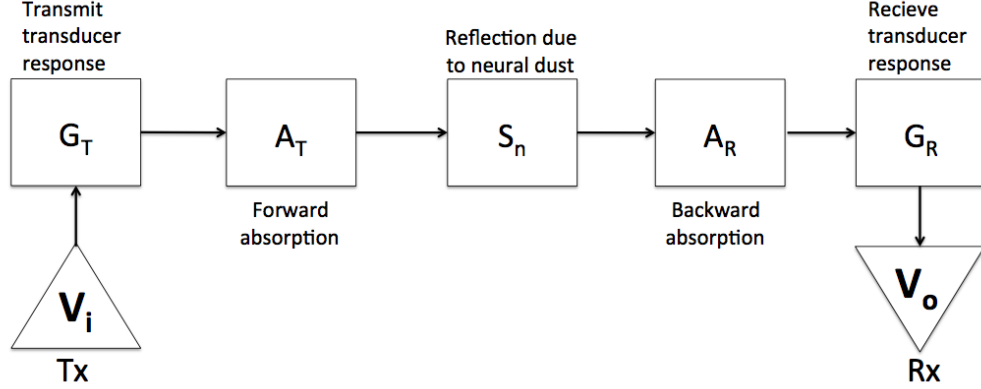


Figure 2.1: System block diagram for ultrasonic backscatter interrogation system with implantable sensor as a series of frequency blocks

2.2 Losses in Tissues

Acoustic waves experience absorption in tissue that can have major effects on a pulse echo system. The expression for loss in tissue for a single-frequency (f_c) plane wave can be expressed by the following equation:

$$A(z, t) = A_0 \exp(i(\omega_c t - kz)) \exp(-\alpha z) \quad (2.3)$$

where A_0 is the initial amplitude of the propagation wave, ω_c is the carrier frequency in radians per second, k is the wave number, and α is the attenuation factor described in units of nepers. Equation 2.3 shows that tissue absorption has a power law dependance on frequency, indicating acoustic pulses not only become smaller in amplitude but also change shape. To accurately understand the model for ultrasonic backscatter interrogation, it is imperative to define a model to understand the effect of absorption on acoustic waveforms in tissue. This section describes absorption models that may be analyzed in the time or frequency domains [36].

Losses in tissue observe a frequency power law defined as

$$\alpha(f) = \alpha_0 + \alpha_1 |f|^y \quad (2.4)$$

where α_0 is often zero and y is a power law exponent. Additionally the phase velocity of tissue also varies with frequency as shown below,

$$c(f) = c_0 + \Delta c(f) \quad (2.5)$$

where $\Delta c(f)$ is a small change in sound speed with frequency. However, this change in phase velocity is negligible in most cases and can often be ignored, as is the case for the model used in this work for ultrasonic backscatter interrogation.

2.2.1 The Material Transfer Function

The material transfer function (MTF) describes the combined effect of absorption and dispersion on acoustic pulse propagation as described by equation 2.6 in the frequency domain [36].

$$MTF(f, z) = \exp(\gamma_T(f) z) \quad (2.6)$$

where $\gamma_T(f)$ is described by

$$\gamma_T(f) = -\alpha(f) - i[k_0(f) + \beta_E(f)] \quad (2.7)$$

where $k_0 = \omega/c_0$ is a baseline wavenumber (c_0 is a sound speed value taken at the center frequency of the spectrum of a pulse) and $\beta_E(f)$ is an excess dispersion term required by causality to include macromolecular effects. $\beta_E(f)$ is the Hilbert transform of $\alpha(f) - \alpha_0$:

$$\beta_E(f) = \frac{-1}{\pi f} * [-\alpha(f) + \alpha_0] \quad (2.8)$$

Due to the Hilbert transform integral of the power law absorption, the numerical value of equation 2.8 increases monotonically with frequency creating evaluation problems. A time casual relation may be used to solve this issue, resulting in different solutions for various values of y [36]. For y as an even integer or noninteger,

$$\beta_E(f) = \alpha_1 \tan\left(\frac{\pi y}{2}\right) f|f|^{y-1} \quad (2.9)$$

and for y as an odd integer,

$$\beta_E(f) = -\left(\frac{2}{\pi} \alpha_1 f^y \ln|y|\right) \quad (2.10)$$

for the case of tissue in this model $y = 1$.

2.2.2 The Material Impulse Response Function

The material impulse response function, $mirf(t)$, is used to describe the time domain absorption in tissue and is found by taking the inverse Fourier Transform of the material transfer function [36].

$$mirf(t, z) = \mathcal{F}^{-1}\{\exp(\gamma_T(f) z)\} \quad (2.11)$$

Defining the $MTF(f)$ and $mirf(t)$ allows for time domain or frequency domain analysis of a pulse signal in tissue. For an initial pulse described by $p_0(t)$ with a spectrum of $P_0(f)$, the pulse at distance z can be described in the time domain by

$$p(t, z) = p_0(t) * mirf(t, z) \quad (2.12)$$

or the frequency domain by

$$P(f, z) = P_0(f)MTF(f, z) \quad (2.13)$$

To simplify large systems using two port analysis from network theory, the MTF was constructed as an ABCD matrix

$$M_{tissue} = \begin{bmatrix} \cosh(\gamma_T d) & Z_T \sinh(\gamma_T d) \\ \sinh(\gamma_T d)/Z_T & \cosh(\gamma_T d) \end{bmatrix}$$

where Z_T is the load impedance from the adjacent network [36].

2.3 Transducer Model

The ultrasonic interrogation system consists of two transducers in the communication chain: the external interrogation transducer and the implant transducer. For modeling the transducers in the ultrasonic link, the KLM model, a thickness-expander model introduced by Krimholtz, Leedom, and Matthaei, was used [37]. The KLM model provides advantages by separating the acoustic and electrical parts of the transducer. The equivalent circuit model is shown in figure 2.2. The KLM model consists of three main parts: an electrical port and two acoustic groups extending to the left and right from the center junction of the electrical group. This gives the advantage of isolating each port in the analysis: Port 1 is used to represent forward transmission of acoustic energy into a medium, port 2 is used for acoustic backing, and port 3 is the electric port of the model. Network theory is utilized to represent the equivalent circuit model as 2 x 2 ABCD matrices to easily derive the overall transfer function for the interrogation system [36].

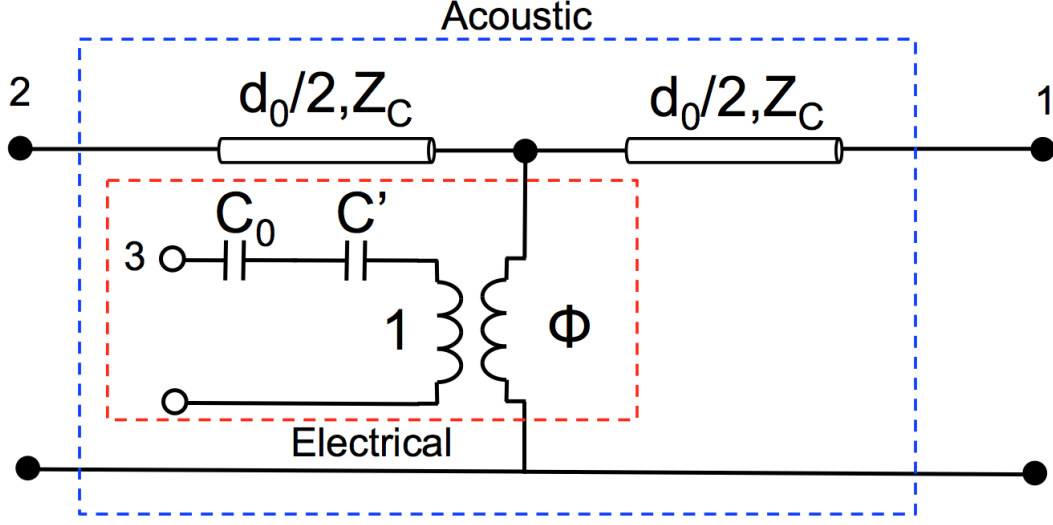


Figure 2.2: Schematic representation of KLM transducer model

The two capacitive elements inside the electrical port represent the electrical reactance, C_0 , and the current contribution to the acoustic output, C' ,

$$C' = \frac{-C_0}{k_t^2 \text{sinc}(\omega/\omega_0)} \quad (2.14)$$

where k_t is the thickness expander mode coupling constant. The transformer between the electrical and acoustic ports converts electrical signals to acoustic waves with a turn ratio described by

$$\phi = k_t \left(\frac{\pi}{\omega_0 C_0 Z_C} \right)^{(1/2)} \text{sinc}[\omega/(2\omega_0)] \quad (2.15)$$

where Z_C is the normalized impedance of the crystal. The node connecting the electrical port and the acoustic ports is placed in the center point of the transducer, creating two acoustic layers each with thickness $d_0/2$.

2.4 Scattering

Information from the implantable sensor is encoded on the acoustic backscatter signal due to scattering from the acoustic boundary of tissue and the implanted

sensor. Various models for scattering exist for acoustic boundaries based on the type of boundary; however, for boundaries that are much greater than the wavelength of the acoustic wave, specular scattering is appropriate. Specular scattering can be approximated by rays incident on the object, such that the scattered wavefront is approximately a replica of the shape of the object. The wavefront of the implantable sensor can be approximated as a rectangle with length, a , and width, b . As acoustic waves hit the boundary of the implantable sensor, the waves see a cross-sectional area of $a \times b$, resulting in an acoustic reflection determined by an impedance mismatch between the propagation medium and implant as described by a reflection factor (RF) [36]. The overall backscatter intensity (I_r) at distance r to the incident intensity (I_i) can be described as

$$\frac{I_r}{I_i} = \frac{ab}{4\pi r^2} |RF|^2 \quad (2.16)$$

The reflection factor is used to find the energy reflected back to the source due to impedance mismatch of two boundaries. This method requires the input impedance of each boundary to be found, which can be simplified by representing the system in terms of ABCD matrices. With the impedances known, the reflection factor of two boundaries with incident angles θ_1 and θ_2 can be expressed by equation 2.17.

$$RF = \frac{Z_2 \cos \theta_1 - Z_1 \cos \theta_2}{Z_2 \cos \theta_1 + Z_1 \cos \theta_2} \quad (2.17)$$

2.5 Ultrasonic Communication Link Model

Figure 2.3 shows the equivalent circuit model used for the complete backscatter interrogation model. The system utilizes the KLM model for the external interrogator's transducer as well as the transducer element of the implanted sensor. To model the backscatter modulation due to neural modulation, a variable termination impedance Z_{neural} is attached across the electrical port of the implantable sensor. This variable impedance effectively changes the input impedance of the implant, which consequently changes the reflection coefficient at the boundary of the tissue and implant. Therefore, this change in reflected energy at the tissue/ implant boundary due to Z_{neural} modifies the amplitude of the backscatter signal, encoding the neural information. To find the input impedance of the each boundary ($Z_{implant}$ and Z_{T_in}) impedances in the network of matrices are found in a sequential manner starting with the terminating impedance and working inwards:

$$Z_{n-1} = \frac{A_{n-1}Z_n + B_{n-1}}{C_{n-1}Z_n + D_{n-1}} \quad (2.18)$$

With the input impedance of each boundary found the reflection coefficient can be represented. Similarly, the transfer function for each section of the equivalent model can be found with cascading two port networks:

$$\frac{V_n}{V_{n-1}} = \frac{Z_n}{A_{n-1}Z_n + B_{n-1}} \quad (2.19)$$

The process results in the overall transfer function of the system as shown in equation 2.20 [38].

$$\frac{V_N}{V_1} = \frac{V_2}{V_1} \frac{V_3}{V_2} \cdots \frac{V_{N-1}}{V_{N-2}} \frac{V_N}{V_{N-1}} \quad (2.20)$$

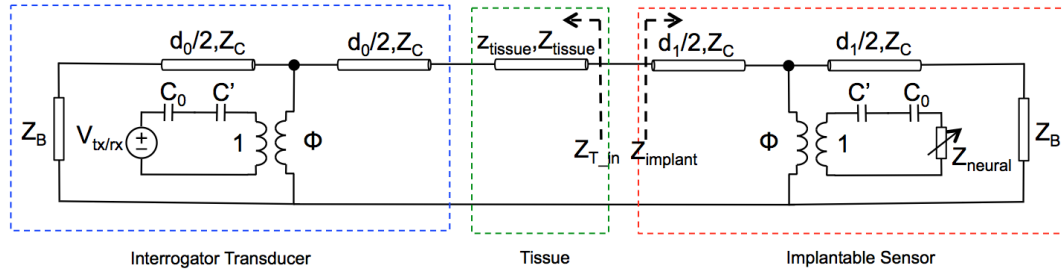


Figure 2.3: Equivalent circuit for complete ultrasonic link model

2.6 Simulation Results

The system model was used to simulate the behavior of the ultrasound backscatter interrogation system. Although a transducer array will most likely be used in practice for the interrogator's external transducer, a single lead zirconate titanate (PZT) element with 2.5 mm length and 2.5 mm width is used in the model to understand trends in ultrasound backscatter communication. A single PZT element with 1.3 mm length and 1.3 mm width is used for the implant's transducer. Both transducers are established with a 1.8 MHz center frequency by introducing a bandpass filter into the system model. The normalized crystal impedance, Z_C , and the backing material impedance, Z_B , are set to 60 MRayls and 6 MRayls respectively for both transducers.

A distance of 10 mm is set between the external transducer and the implantable sensor. The figures below show the time domain simulation results for the ultrasonic backscatter interrogation system. The system is driven by a six pulse, 32V square wave at 1.8 MHz shown in figure 2.4. Figure 2.5 shows the received electrical signal from the ultrasonic backscatter interrogation simulation when Z_{neural} is in both the open circuit and short circuit configurations. The amplitude of the received signal is adjusted by a scaling factor found empirically.

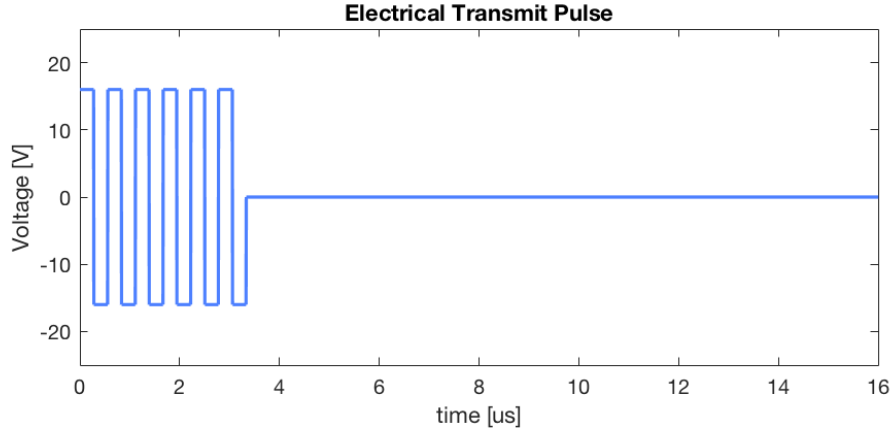


Figure 2.4: Electrical excitation pulse

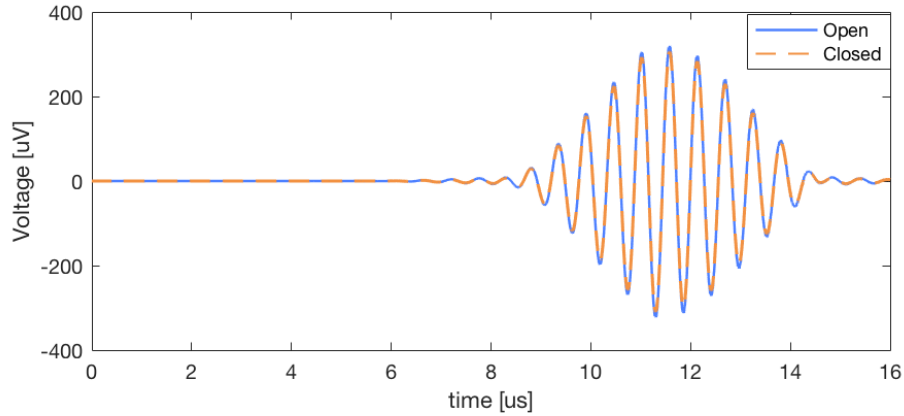


Figure 2.5: Received electrical backscatter signal with dust mote open and closed, respectively

Figure 2.6 shows the normalized amplitude of the received signal simulated at differ-

ent neural impedance modulations. Considering a two state modulation system in which Z_{neural} is either a short circuit or an open circuit, the receive signal modulates by 3.64%.

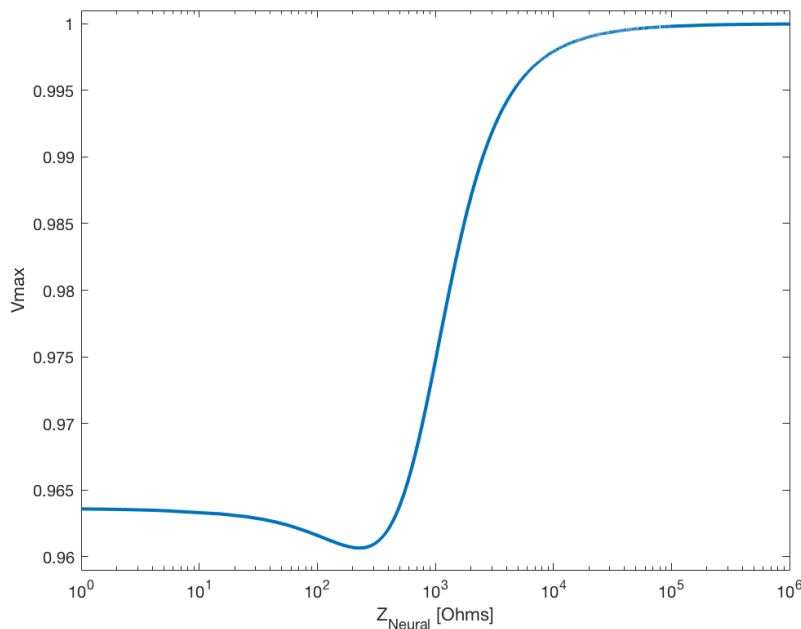


Figure 2.6: Normalized backscatter peak amplitude versus neural modulation at $f = 1.8$ MHz

2.7 Discussion

The ultrasonic link model demonstrates the principles behind ultrasonic backscatter interrogation. The simulated modulation depth of 3.64% illustrates the system's ability to detect a digital encoding scheme where a high level corresponds to an open circuit across the mote's transducer electrodes and a low level corresponds to a closed circuit across the mote's transducer electrodes. Additionally, the maximum modulated depth of 4.0% occurs at the mote's matched input impedance of 225Ω . Modulating Z_{neural} between the matched impedance and an open circuit provides greater modulation depth but is more difficult to implement in practice than simply opening and shorting the electrodes. Figure 2.7 shows the simulated backscatter modulation depth after scaling for amplification and the measured backscatter modulation depth

after amplification. The measured modulation depth of 6.45% is greater than the expected modulation depth of 3.64% indicated by the ultrasonic interrogation link model.

Probable sources of disparity in the system model originate from the model's exclusion of acoustic matching layers, neglect to address individual transducer array elements, and assumption of the transducer thickness expansion mode. Neglect of the transducer's acoustic matching layers results in additional acoustic loss while increasing model simplicity. Likewise, modeling a transducer array as one large transducer may over simplify the array's complex acoustic beam pattern but provides an effective compromise in model complexity and accuracy. Finally, because the KLM model assumes planar dimensions which exhibit purely one-dimensional thickness vibration, the characteristics of the dust mote's miniaturized transducer deviate from the behavior predicted by the KLM model. 3D finite element simulation software is necessary for a more accurate and involved transducer model of the miniaturized transducer elements. Despite some discrepancies, the correlation between the system model and the experimental results indicates the usefulness of the transfer matrix method derived using the KLM model and material transfer function for representing an ultrasonic interrogation link's sensitivity to electrical load impedance.

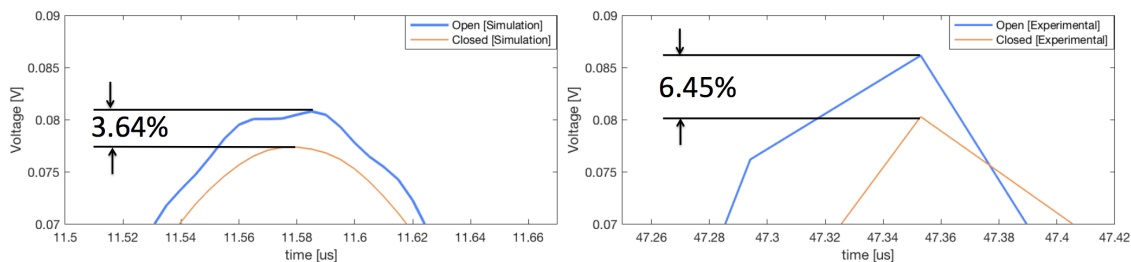


Figure 2.7: Comparison of simulated modulation depth (left) and measured modulation depth (right)

Chapter 3

System Architecture

3.1 Requirements

Neural interface hardware needs to be portable and compact, operate in real time, and be validated with long term experimentation for brain machine interfacing systems to be used for practical applications. Therefore, a wearable neural signal acquisition device must be designed to enable safe, closed-loop neuromodulation experimentation in *in-vivo* environments. To achieve this goal, an ultrasound backscatter interrogator that supports real-time backscatter processing in a rodent-wearable, completely wireless device is designed. Designing a wearable system for a rodent presents unique constraints on the size and weight of the system. The size of the rodent wearable system is constrained to 38 mm x 56 mm while the weight of the system is limited to 40 g (10% of an average male rodent's mass) to ensure unimpeded movement of the rodent [39]. Figure 3.1 shows a 3D rendering of the constrained system worn by an average sized rat. Additionally, the system is required to operate for at least one hour in order to conduct proper experiments to validate the wireless ultrasonic backscatter interrogation system. The battery life constraint creates a need for low power devices. Additionally, this need for low power electronics is compounded by undesired extra weight and volume of large batteries needed for high power designs.

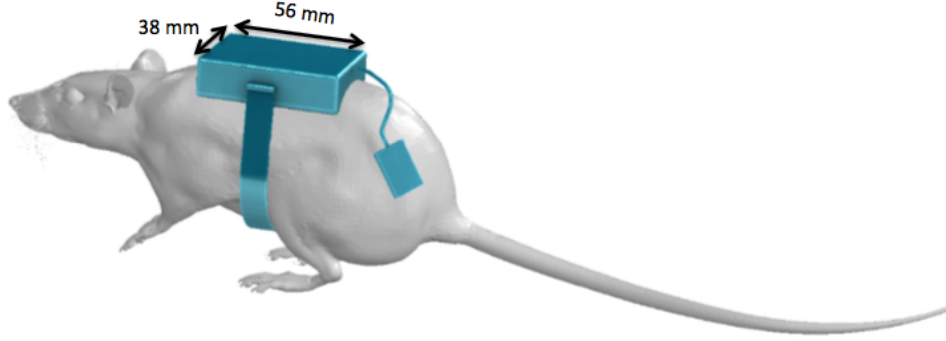


Figure 3.1: Mock system worn by rat

To enable closed loop neuromodulation experiments, the device requires real time operation. Merely collecting raw ultrasonic backscatter data with the inability to interact with client devices in real time limits the device as a neural recording system. Raw data can be stored off the device and processed by a higher performance computer, but the large amount of raw data in ultrasound systems impose limitations on wireless transmission needed for an untethered device. Typical ultrasonic interrogation systems reach data rates of 80 Mbps, which exceeds the 25 Mbps data rate for Bluetooth 4.0 typically used for mobile devices. Therefore, the wearable ultrasound system must be able to seamlessly communicate wireless, preprocessed ultrasonic backscatter information to a variety of devices. Although various techniques may be applied on chip to reduce the data rate of ultrasound systems, evolving implantable sensor technologies require ultrasonic backscatter interrogation systems with flexible digital signal processing (DSP) capabilities. A microcontroller solution provides the most flexible processing capabilities over other solutions. Moreover, a fairly high performance microcontroller with a dedicated DSP core is desired to enable efficient signal processing.

Proper analog signal conditioning of the backscatter signal is required to ensure adequate data extraction. Simulation and empirical data results indicate the expected amplitude range for the backscatter signal is in the range of $125\mu\text{V}$ - $400\mu\text{V}$ with an expected modulation depth of 2.5% to 6.5%. Additionally, the carrier frequency for the system is determined to be 1.8 MHz based on transducer resonance. For accurate processing of the backscatter signal oversampling of at least five times the 1.8MHz carrier frequency is required. Therefore, the ADC used to capture the backscatter signal requires a sampling rate of at least 9.0 MHz.

3.2 System Overview

Table 3.1: Design Parameters

# Transducer elements	9
# Transmit and Receive Channels	3
# Transmit only channels	4
ADC Sampling Rate	17 Msps
ADC Precision	12-bit
High Pass Filter	660 kHz
Low Pass Filter	7.2 MHz
Battery Capacity	400 mAh
Expected Battery Life	1.25 hrs
Enclosure Size	51 mm x 34 mm x 23 mm
Total Mass	36.9 g

Figure 3.2 depicts the block diagram of the proposed wearable ultrasound interrogation system. The ultrasound link is interfaced by a transducer array, which is driven by the 7-channel high-voltage ultrasound interface ASIC. The system is controlled by a microcontroller which digitizes and processes the backscatter waveform and sends demodulated data to a client through a bluetooth module.

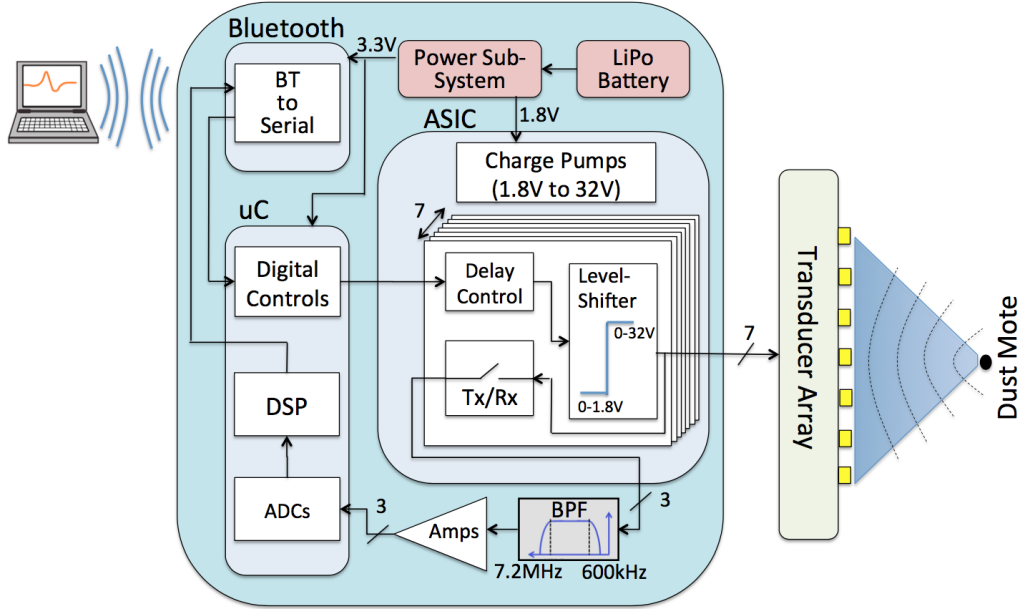


Figure 3.2: System Block Diagram

3.3 Electronics

Powered by a 400 mAh lithium polymer battery, the system consists primarily of a microcontroller, an ultrasound interface ASIC, analog conditioning circuitry, and a Bluetooth transceiver. The wearable ultrasound system requires high speed signal generation for transducer excitation, fast data capture capabilities for backscatter digitization, and efficient DSP performance for real-time processing. To meet these design requirements, the system takes advantage of NXP’s LPC4370 microcontroller. An Arm Cortex-M4 based microcontroller running at frequencies up to 204 MHz, the LPC4370 microcontroller supports single-cycle DSP and single instruction, multiple data (SIMD) instructions, includes an 80 Msps 12-bit ADC, and comes in a 100-pin 9 x 9 mm² ball grid array (BGA) package.

The ultrasound ASIC, operated with a single 1.8V supply, generates a 0-32V square wave to independently actuate 7 piezoelectric transducers using integrated charge pumps and level shifters [40]. Packaged in a small 9x9 mm² 64-pin QFN package, the ASIC provides high efficiency power transfer of $\sim 32.5\%$ from the 1.8V supply to the 32V output voltage. The ASIC’s high efficiency power transfer for ultrasound interfacing is explained in prior work [35].

The ASIC employs a transmit/receive switch that isolates electrical feed-through while receiving the backscatter signal from the dust mote. Off-the-shelf operational amplifiers provide 46 dB of gain. A bandpass filter is applied with cutoff frequencies of 660 kHz and 7.2 MHz before the signal is digitized by the microcontroller’s on-chip ADC. The receive signal is over-sampled at 17 Msps to provide adequate resolution for accurate signal processing. Once in the digital domain, real-time backscatter modulation extraction generates a 32-bit demodulated value for each pulse.

This result is sent to the Bluetooth module (HC-06) over universal asynchronous receiver/transmitter (UART) at a baud rate of 115,200. The Bluetooth module sends the data to the remote client using Bluetooth’s synchronous serial port (SSP) protocol. A graphical user interface (GUI) operating on the client device enables convenient user operation of the system. Developed in Matlab, the GUI allows the remote client to connect to the wireless device, set system parameters, choose modes of operation, and display received data in real-time.

3.4 Printed Circuit Board

The physical constraints placed on the ultrasound system to permit awake, unconstrained rodent experimentation involves careful printed circuit board (PCB) design. As a high-speed, mixed signal design, many PCB characteristics such as impedance tolerances, signal integrity, and power subsystem design are considered. With digital signals operating in the range of a few hundred megahertz, ensuring all signals arrive at the desired load with adequate quality to insure proper logic operation is vitally important. Additionally, the area constraint for the PCB creates challenges in isolating analog and digital signals and power supplies.

3.4.1 Signal Integrity

Ultrasonic signal transmission requires high speed pulse excitation patterns and clocks generated from the LPC4370 microcontroller. These signals are realized with a custom protocol utilizing the LPC4370’s serial general purpose input output (SGPIOs) ports that operates up to 100 MHz. Because of the fast switching behavior of these signals, the PCB is constrained to minimize expected signal overshoot, which can degrade signal integrity for misrepresented logic states if ignored. To quantify this effect, a transition electrical length (TEL) is established as the worst case rise or fall time of the digital signal multiplied by the velocity of the signal along the transmission line. For the digital SGPIOs, the worst case rise or fall time is 510 ps, resulting in a TEL of around 750 mm. From this quantity, a design rule is established

for digital signals where traces are constrained to 1/4TEL; therefore, for the SGPIO signals, the trace lengths are kept under 190 mm [41]. To minimize digital interference of the sensitive analog backscatter signals, rules were established to isolate analog signals from digital signals. A crosstalk coefficient is established to constrain spacing between analog and digital traces as

$$CT = \left(\frac{1}{1 + \left(\frac{S}{H}\right)^2} \frac{T_{RT}}{T_R} \right) \quad (3.1)$$

where S is the spacing between traces, H is the substrate height, T_R is the rise time, $T_{RT} = 1.017\sqrt{\epsilon_r 0.475 + 0.067} L^2$, and L is the length of trace overlap. The desired crosstalk coefficient to ensure adequate signal integrity is found to be -66 dB, translating to 0.2 mm of separation between analog and digital traces [42].

3.4.2 Power Subsystem

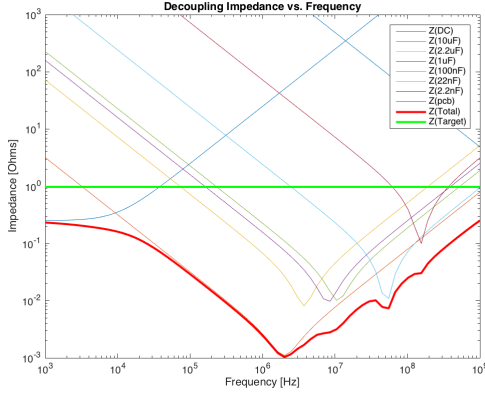
The power subsystem needs to deliver adequate voltage to the load circuits for all operating conditions. Ideal power subsystems deliver constant voltages to the loads independent of load current fluctuations; however, because real DC/DC converters only have low output impedances at low frequencies, embedded systems with dynamic load currents require filters for clean power supplies. Additionally, large current spikes due to simultaneous switching of a large number of digital flip flops in ASIC clock trees results in a load frequency spectrum that is much higher than the clock frequency. To ensure adequate power supply noise, the power distribution requirements are calculated by identifying the allowable voltage change based on PSRR and signal tolerance to noise and the maximum current change for each supply [41]. The power requirements are summarized in table 3.2.

Table 3.2: Power Distribution Requirements

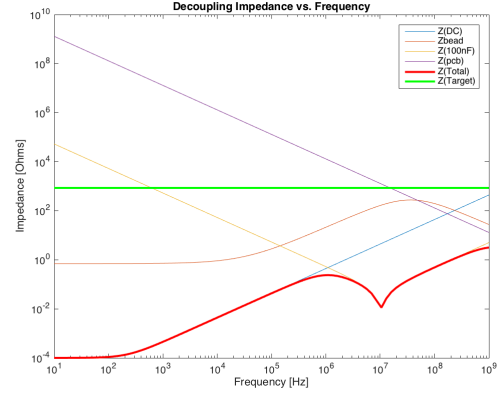
Voltage	AC Ripple		
	Allowable Voltage Drop (mV)	Max Ripple (mA)	Required Impedance (Ω)
3.3 V (Digital)	66.0	22.7	0.97
3.3 V (Analog)	550.0	0.65	850
1.8 V	2.8	0.43	6.6
0.75 V	196.0	0.12	1,640

Given the operating frequency of the LPC4370 at 204 MHz, each power supply is

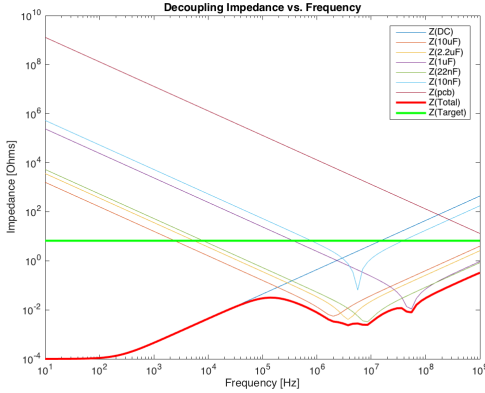
required to work at a frequencies an order of magnitude greater than the operating frequency (1 GHz). Modeling the power distribution as a distributed network of capacitive, inductive, and resistive elements based on the PCB's microstrip transmission lines, decoupling capacitors, and ferrite beads, the output impedance of the power plane for each supply is designed to reject electromagnetic interference and deliver adequate voltage to the load circuits up to 1 GHz (figure 3.3).



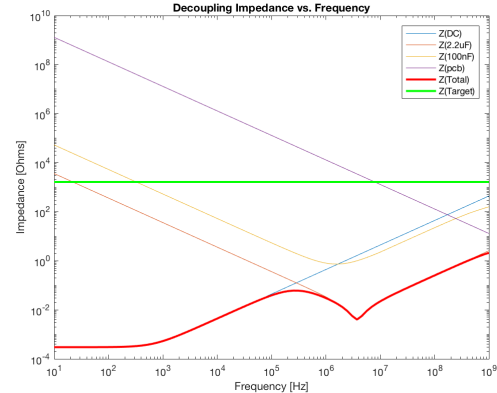
(a) Impedance vs. frequency for 3.3V digital supply



(b) Impedance vs. frequency for 3.3V analog supply



(c) Impedance vs. frequency for 1.8V supply



(d) Impedance vs. frequency for 0.75V supply

Figure 3.3: Simulation of power plane impedance vs. frequency

3.5 Transducer

The ultrasound transducer consists of a 7-channel 3x3 array of bulk PZT active elements in a low-profile, flexible package. In order to achieve a small transducer, the array was fabricated on a flexible-printed-circuit substrate. This approach has been shown to yield good acoustic performance in space-constrained and flexible designs [43] [44]. A custom ultrasound field simulation program was developed with Matlab to design the array geometry and optimize for two competing design goals: (1) maximization of acoustic power delivered to the implanted mote, and (2) minimization of the system’s sensitivity to misalignment. The simulation used a 2-dimensional sinc function to approximate the beam pattern of each square element and complex superposition to calculate the field of the array [45] [46]. Figure 3.4 shows the simulated beam pattern of custom flex transducer with uniform phase across elements. At 14 mm distance, the full-width half-maximum of the array’s beam is 4.78 mm yielding a region over 6 times the dimension of the mote of relatively constant power. This lessens the sensitivity of the ultrasonic link to misalignment. The final geometry was calculated to be 750 μm x 750 μm x 750 μm cubic elements with 1.05 mm center-to-center spacing.

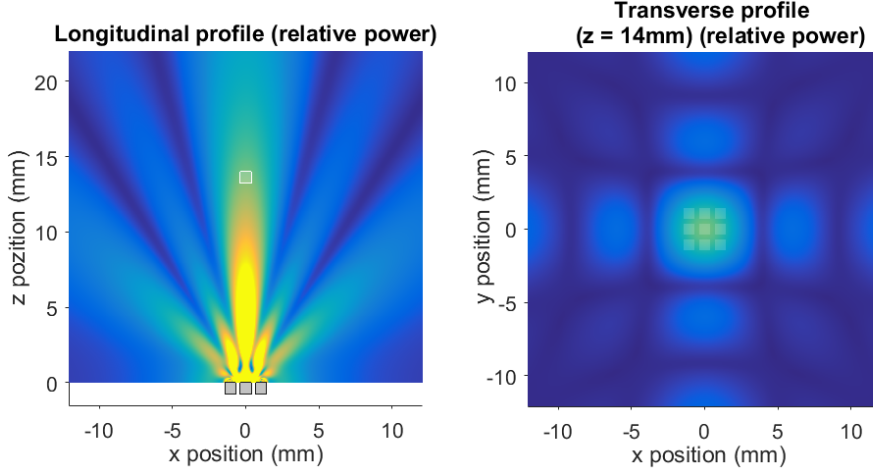


Figure 3.4: Simulated beam pattern of custom flex transducer with uniform phase across elements. Gray squares on the left and white overlaid squares on the right are transducer elements and the white box on the left is the dust mote position.

The transducer’s flexible printed circuit substrate (fabricated by AltaFLEX, Santa Clara, CA) addresses each active element through traces on the back side of the substrate with a via positioned under each element (Figure 3.5). Of the nine physical

elements, three are independent transmit-receive elements, three are independent transmit-only elements, and three are electrically shorted transmit-only elements. After substrate manufacturing, a pre-metallized PZT disk (841, APC International) is diced to the size of the aperture of the array and bonded to the substrate with conductive silver epoxy (EPO-TEK 301, Billerica, MA). The elements are then diced in-place to form the array (DISCO DAD3240 Automatic Dicing Saw, Tokyo, Japan). A layer of metalized polyester film (DURA-LAR aluminized PET, Grafix, Maple Heights OH) is then bonded to the top of the elements to provide a common ground and an acoustic matching layer. An absorptive backing layer of tungsten powder filled polyurethane is cured on the back side of the substrate to reduce the ringing of the transducer elements. The material has a 17% volume fraction of tungsten, corresponding to an estimated attenuation of 27 dB/mm [47]. Finally, a protective layer of non-conductive epoxy (EPO-TEK 353ND, Billerica, MA) is cured around the non-acoustically-transmitting surfaces of the transducer for protection.

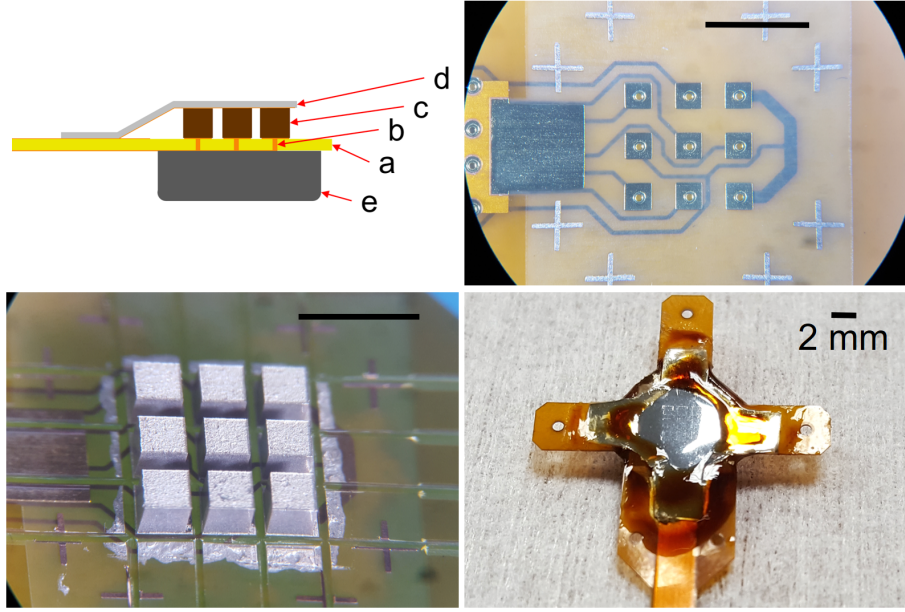


Figure 3.5: (Top left): Cross-section of ultrasound transducer stack-up. [a] flex PCB; [b] vias addressing each array element; [c] PZT active elements; [d] metalized PET layer; [e] absorptive backing layer of tungsten powder - filled polyurethane. (Top Right): flexible pcb prior to PZT bonding. (Bottom Left): Active elements after dicing. (Bottom Right): Finished transducer. All scale bars 2 mm.

3.6 Wearable Device Software

The flowchart for the control software on the wearable device is shown in figure 3.6. Upon boot up, the device initializes hardware peripherals such as the system clock, interrupt priorities, UART, GPIOs, and ADC. Next, the device pings the remote client and waits for a response before continuing. With a connection established, the wearable device waits for user defined parameters, such as pulse frequency, pulse duration, adjacent channel delays, mode of operation, and processing mode, to be received from the remote client. With the parameters stored on the device, the SGPIOs are configured to drive the external transducers with the correct pulse excitation pattern. The operation mode received by the client dictates the device behavior. The reset operation command allows the device to accept new user defined parameters from the client. The inactive operation command forces the device into an idle state, requiring the device to be power cycled to become active again. The active operation command triggers the transducer's transmit pulse excitation pattern and begins the ADC capture routine for recording backscatter data. The device transmits the raw backscatter data to the remote client if specified by the user. If the user specifies to process the data, the backscatter modulation extraction algorithm is applied.

The system is designed to detect backscatter modulation within a specified distance range from the transducer. With a known speed of sound (assume 1540 m/s in tissue), signals arriving from this range correspond to those in a time window of the backscatter. This window is called the region of interest (ROI). Discarding data outside of this region avoids transmit drive feed-through and transducer ring-down signals being included in the backscatter demodulation, which improves effective modulation depth. The raw digitized backscatter waveform corresponding to the ROI is first digitally filtered with a 32-tap finite impulse response bandpass filter centered at the carrier frequency of 1.8 MHz with a bandwidth of 0.4 MHz to remove any remaining out-of-band noise after filtering in analog hardware. The device transmits the filtered backscatter data to the remote client if specified by the user. Next, this data is time-windowed with a trapezoidal window such that there is a positive ramp at the beginning and a negative ramp at the end of the data. This serves to lessen the effect of temporal jitter on the outcome of the extraction. Finally, the L1 norm of this data is taken to extract the magnitude of the signal's amplitude within this region. The result of this L1-norm yields the extracted value of backscatter modulation data, which is linearly related to modulated information at the implanted device [1]. The majority of the processing takes place on fixed point data with one sign bit and 15 fractional bits (Q15), and takes advantage of the

CMSIS DSP library to implement the ARM Cortex single-cycle multiply-accumulate and single-instruction multiple-data operations. The resulting extracted backscatter value is a fixed point data type with one sign bit and 31 fractional bits (Q31) and is transmitted to the remote client. After data transmission, the device executes the next operation command until the inactive command is received.

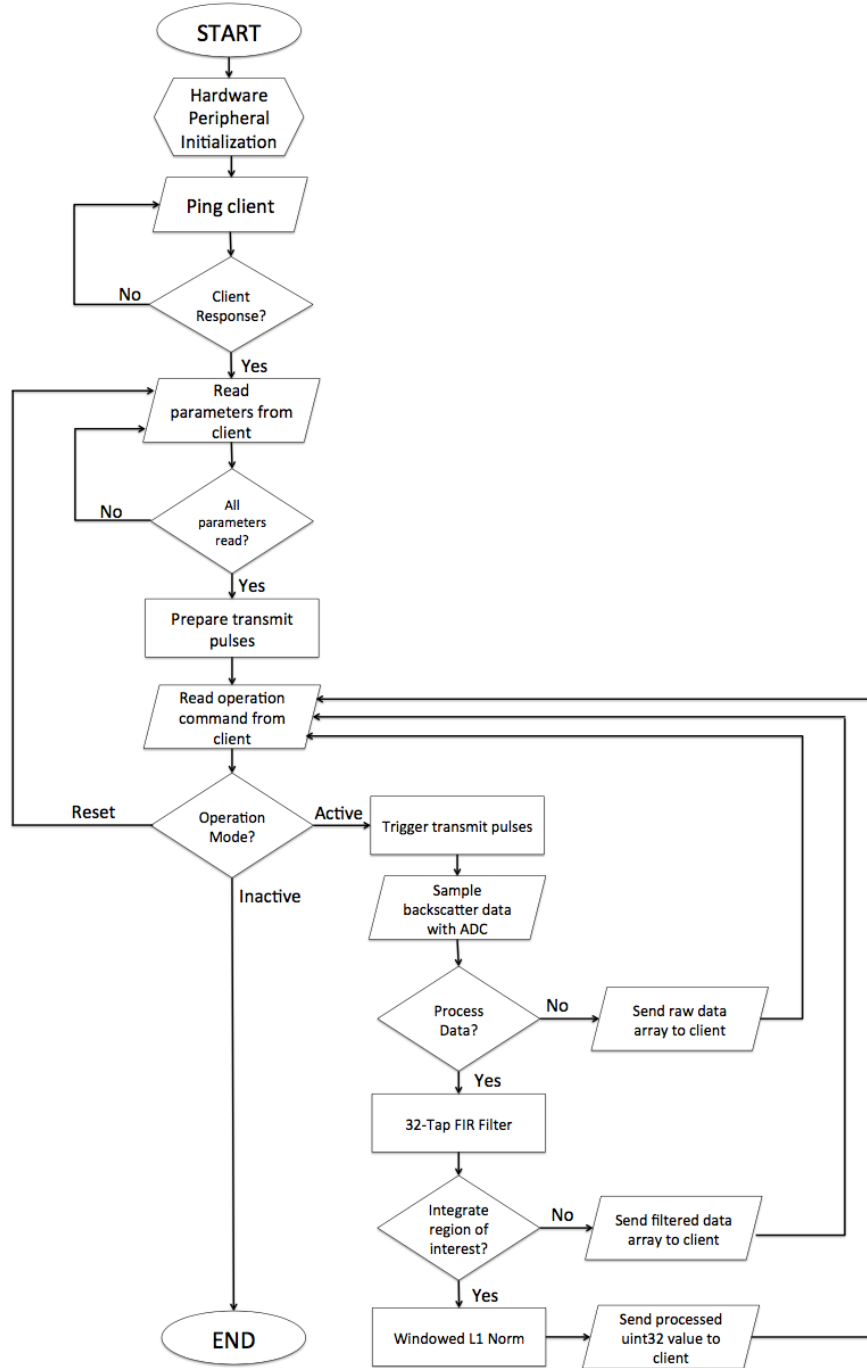


Figure 3.6: Wearable device software flowchart

3.7 Remote Client Software

The flowchart for the control software on the client device is shown in figure 3.6. Once the remote client software is active, a graphical user interface (GUI) shown in figure 3.8 allows the user to define parameters such as pulse frequency, pulse duration, adjacent channel delays, and mode of operation. The remote client waits to connect to the wearable device until specified by the user via the GUI. At this point, the communication port is opened and the client waits for a ping from the wearable device. If the client does not receive a ping within 10 seconds, a timeout is flagged, notifying the user of the error. The GUI allows for remote control of the wearable device's behavior. If the disconnect button is toggled, the client will close the communication port with the device. A popup menu on the GUI decides one of three operation commands to transmit to the wearable device: raw, filter, and process modes. Next, the client will determine if data has been received from the wearable device by checking a first in first out (FIFO) data buffer that handles data received on the communication port. For experimentation, the client also controls neural dust modulation. A predetermined data sequence is established that controls a digitally controlled switch for neural dust impedance variation. The control of this switch can be toggled on or off through the GUI. All incoming data can be saved, requiring a fast save method to minimize system latency. If the client receives processed data from the interrogator device, the extracted modulation value (32 bit unsigned integer) is appended to the end of the current waveform for live data streaming. If the client receives either the filtered or raw backscatter signal, the incoming data replaces the previous waveform and is displayed on the GUI. If the GUI window is closed at anytime, the client disconnects from the interrogator and the program terminates.

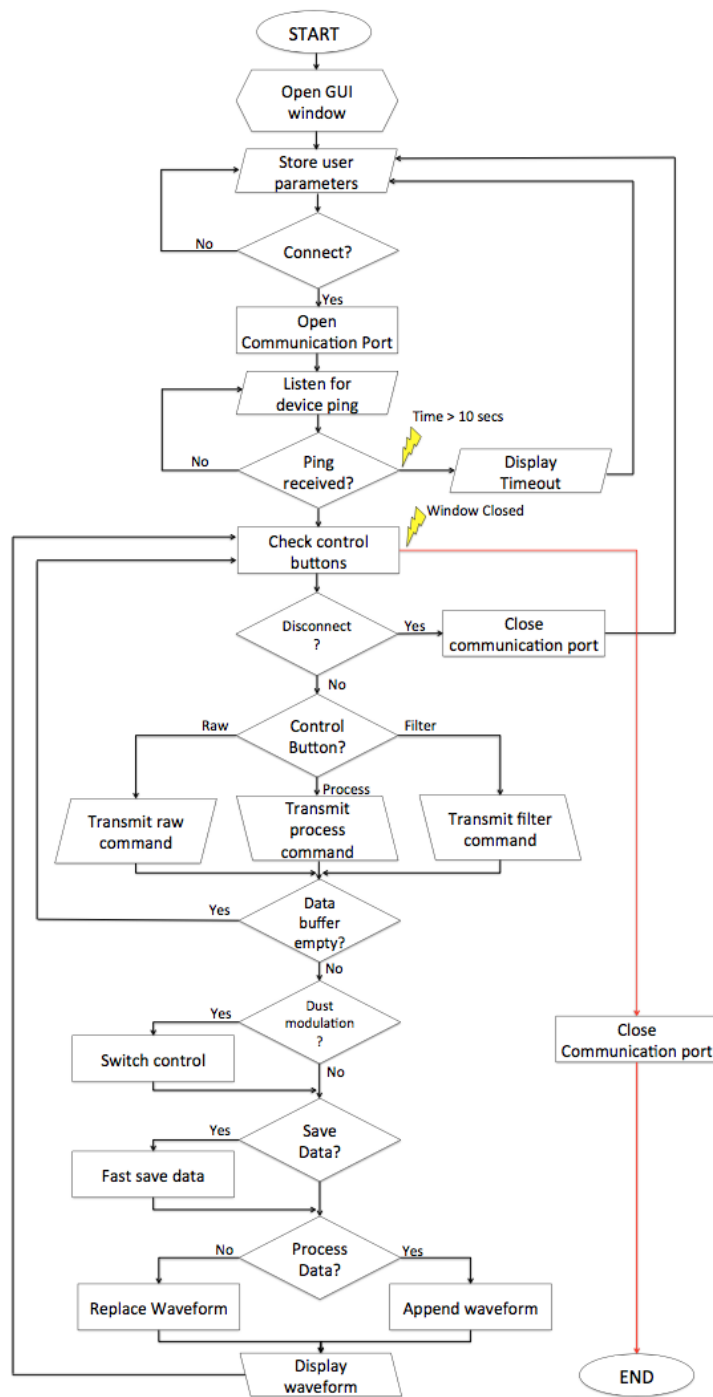


Figure 3.7: Remote client software flowchart

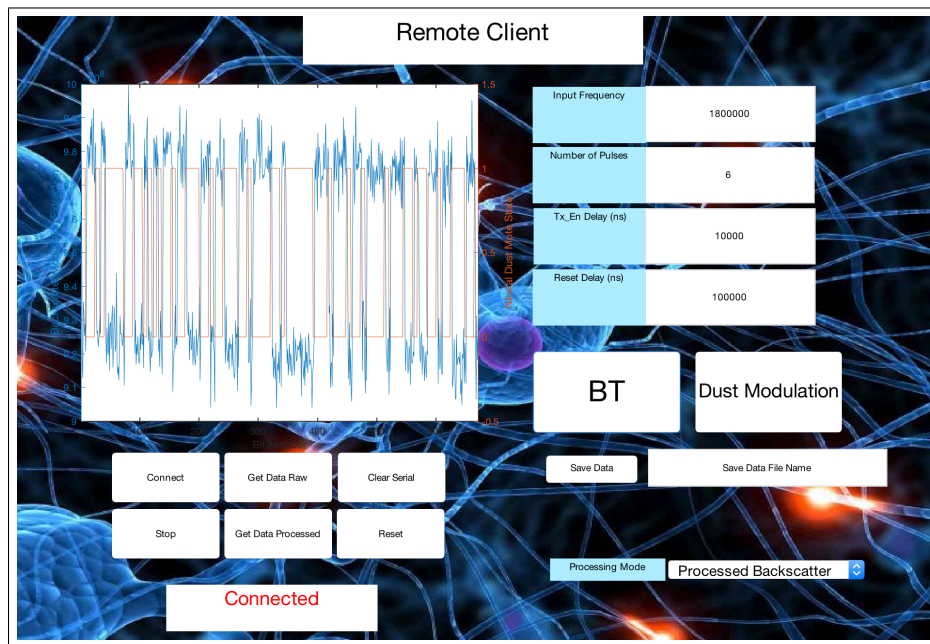


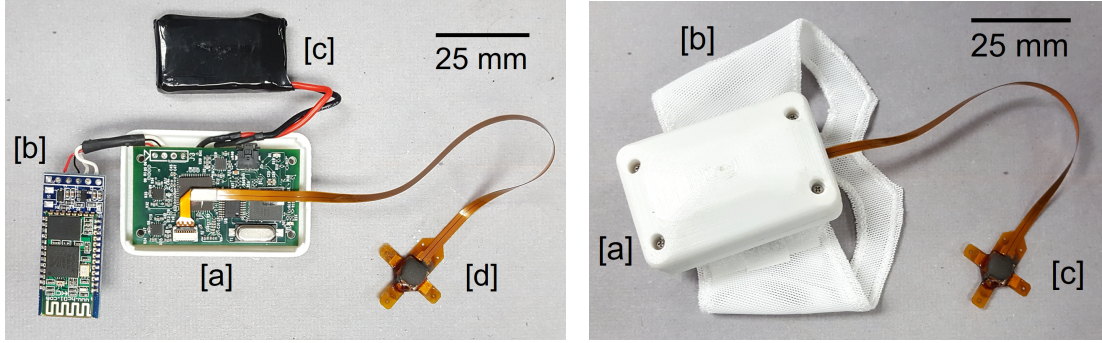
Figure 3.8: Graphical user interface on remote client

Chapter 4

Experimental Verification

4.1 Physical System

The physical design of the wearable system is shown in Figure 4.1. The device is comprised of a custom printed circuit board (PCB) for ultrasound transmit, receive, and processing, a custom flexible PCB to connect the transducer array with the main PCB, a Bluetooth module for wireless transmission, and a lithium polymer (LiPo) battery. These components are shown in Figure 4.1a. The wearable device is housed in the enclosure as shown in Figure 4.1b, and affixed to a rat with a harness extending around the thorax and upper limbs ('Rat Jacket' 620060, Harvard Apparatus, Holliston, MA) shown in Figure 4.2. The enclosure measures 51mm x 34mm x 23mm and the system has a mass of 36.9g, which is under the conservative limit of a 400g rat carrying 10% of its body weight [39]. Animal handling was in accordance with University of California, Berkeley Animal Care and Use Committee regulations.



(a) Interrogator exploded view [a] main board; [b] bluetooth module; [c] battery; [d] transducer
 (b) Assembled interrogator [a] housing; [b] rodent harness; [c] transducer

Figure 4.1: Physical design

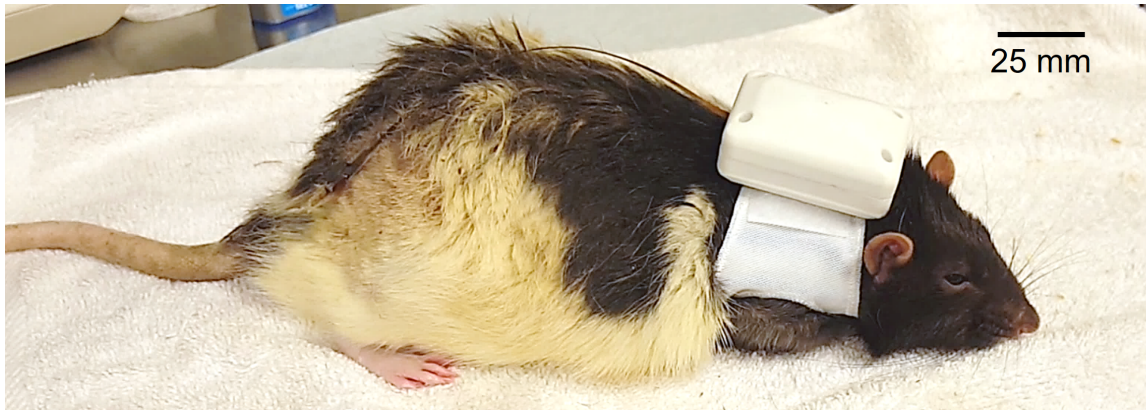


Figure 4.2: Wearable interrogator seen by an adult male Long-Evans rat.

4.2 Experimental Setup

The system is validated with a bench top setup mimicking an *in-vivo* environment shown in figure 4.3. A dust mote [1] and transducer array are placed in ultrasound coupling gel to simulate tissue; ultrasound coupling gel has a similar acoustic impedance compared to tissue of around 1.5 MRayl. Both elements are attached to precision controlled platforms for accurate alignment and placement. The transducer

array is placed 14 mm away from the dust mote, which corresponds to a $18.6\mu\text{s}$ round-trip time of flight assuming an acoustic velocity of $1,540\text{ m/s}$ in ultrasound coupling gel. The transducer array is excited with six 1.8 MHz , $0\text{-}32\text{V}$ square wave pulses, and the backscatter signal is digitized with 2000 samples at 17 Msps and 12-bits of resolution. For time-domain backscatter inspection, complete backscatter waveforms are filtered in real time on the device and sent to the client through a wired, serial connection. In normal operation, the complete modulation extraction algorithm is applied to the backscatter data on the device in real-time, compressing the backscatter signal to four bytes. The processed data is transmitted through Bluetooth's SSP protocol to a remote client and streamed through the GUI in real-time.

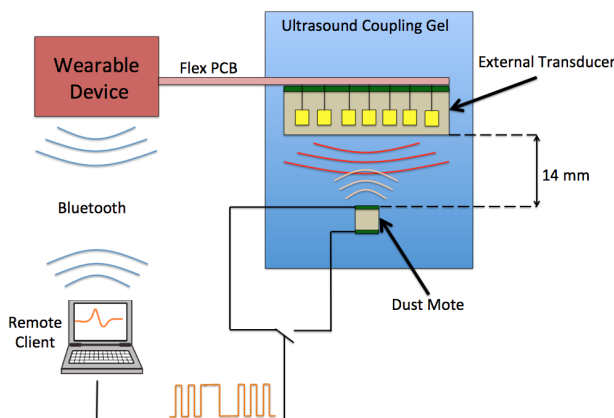


Figure 4.3: Experimental Setup

4.3 Results

4.3.1 Backscatter Signals

Figure 4.4 shows the filtered backscatter signals collected with the described experimental setup. Signals are collected while the dust mote electrodes are in the shorted and opened configurations. The change in impedance due to the switch activity results in a backscatter peak amplitude that is 11.5 mV greater in the open switch configuration, a modulation depth of 6.45% . The long duration of the echo from the mote indicates transducer ringing despite a damping backing layer. While the under-damped transducer system response does spread out the backscatter signal in the time-domain, demodulation is successful as long as the backscatter from the implanted device is captured within the ROI.

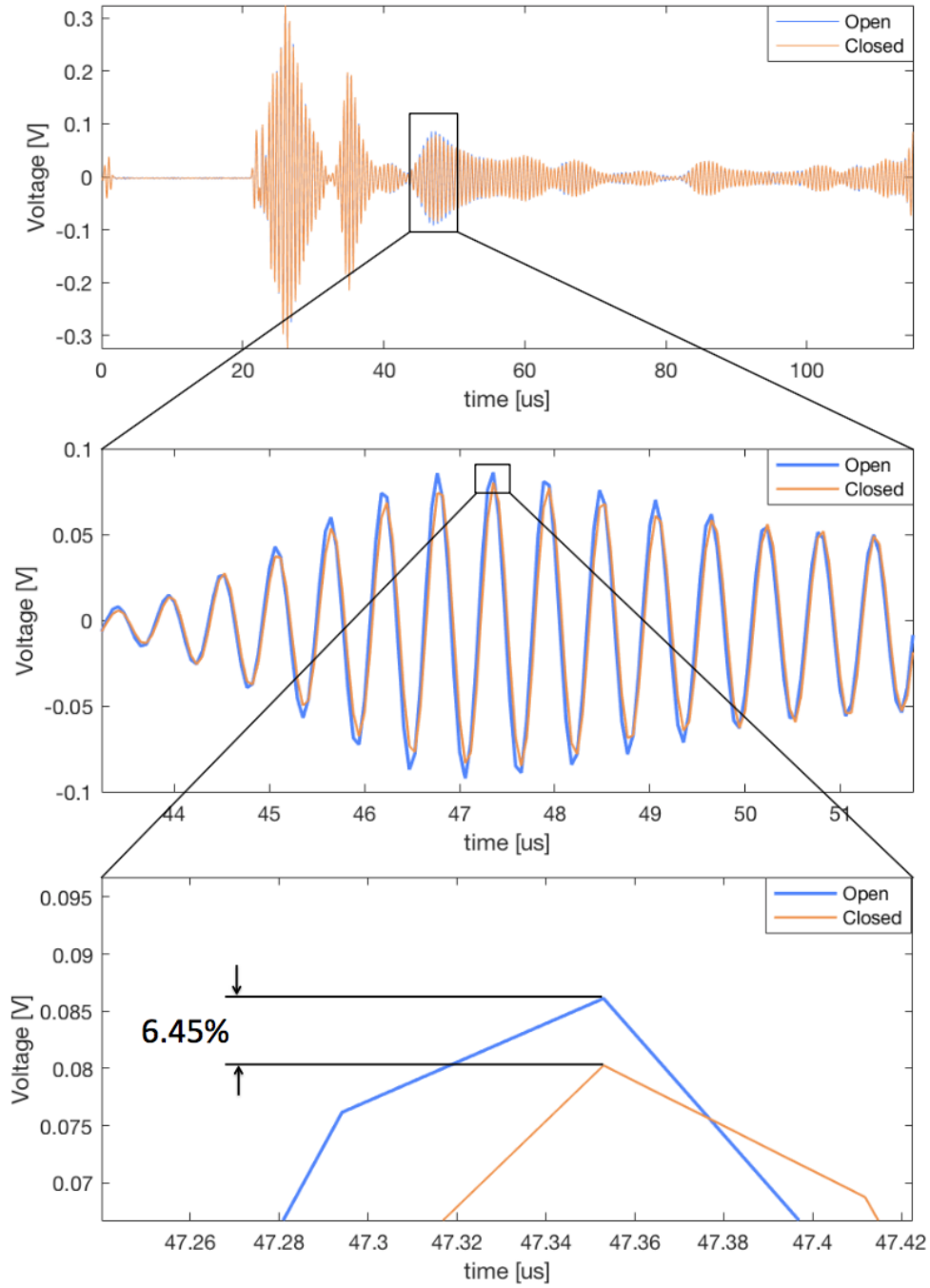


Figure 4.4: (Top) Received signal with dust mote open and closed, respectively. (Middle) Region of interest. (Bottom) Modulation depth.

4.3.2 Neural Dust Mote Modulation Extraction

Using pulse-amplitude-modulated non-return to zero level coding, a backscatter sensor mote is modulated to send a predetermined 11-character ASCII message (“hello world”). The modulation of the device’s acoustic impedance is achieved by shunting the dust mote’s piezoelectric crystal across a digitally controlled switch where a high level corresponds to the open configuration and a low level corresponds to the closed configuration. Figure 4.5 shows the modulated values on the dust mote and the corresponding extracted modulation values of the wearable ultrasound device. The absolute value and noise margin of the extracted signal values depend on a variety of factors such as mote distance, orientation, and size; however, the extracted waveform remains representative of the modulated signal on the dust mote, varying by a linear scaling factor. Improving ROI windows to lessen the effects of backscatter phase shifts is expected to reduce noise of the extracted value.

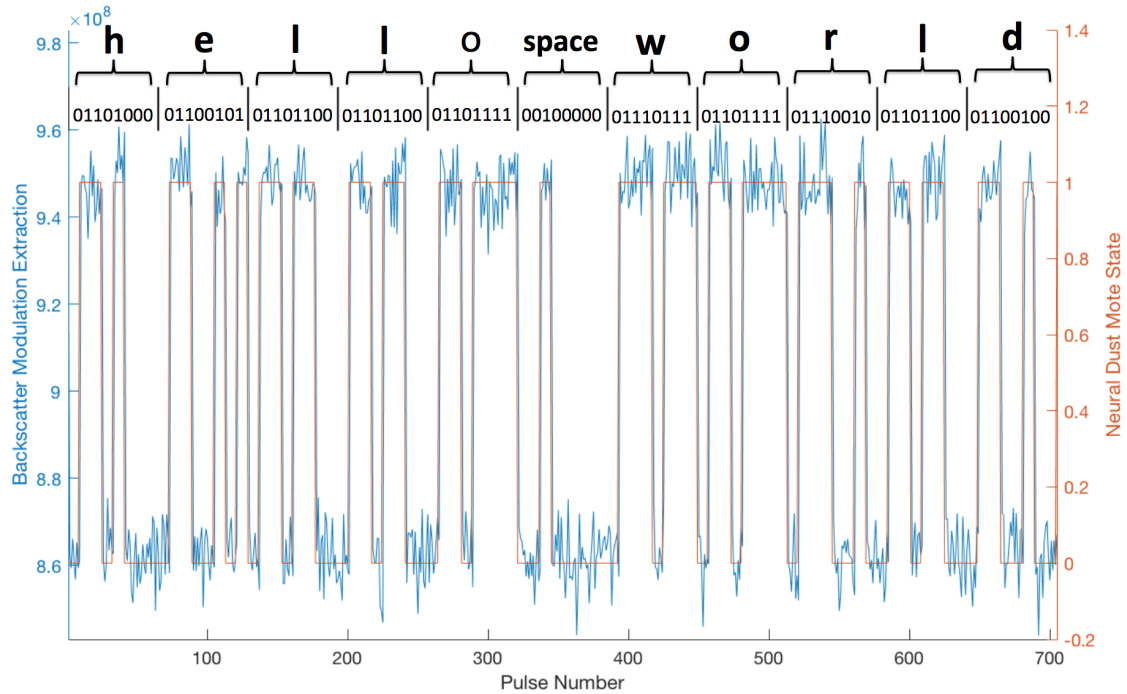


Figure 4.5: Interrogation of “hello world” modulated on neural dust

4.3.3 Bit Error Rate

Bit error rate (BER) is defined as the number of bit errors divided by the total number of transferred bits during a time interval. BER is measured by comparing a predefined modulation sequence on the dust mote against the interrogated extracted values. A logic threshold is established every 100 bits as the mean of the high and low extracted values. Using this method, a BER of 0.16% is observed for 56 kbits of transmitted data with the described experimental setup. Figure 4.6 shows an interrogated extracted value bit error. A small inflation of BER is observed from a slight shift in the dust mote's orientation over time. This effectively reduces the system's noise margin, as the extracted values drift closer to the logic threshold. Nonetheless, the measured BER demonstrates the ultrasonic interrogation system's robustness for wireless communication.

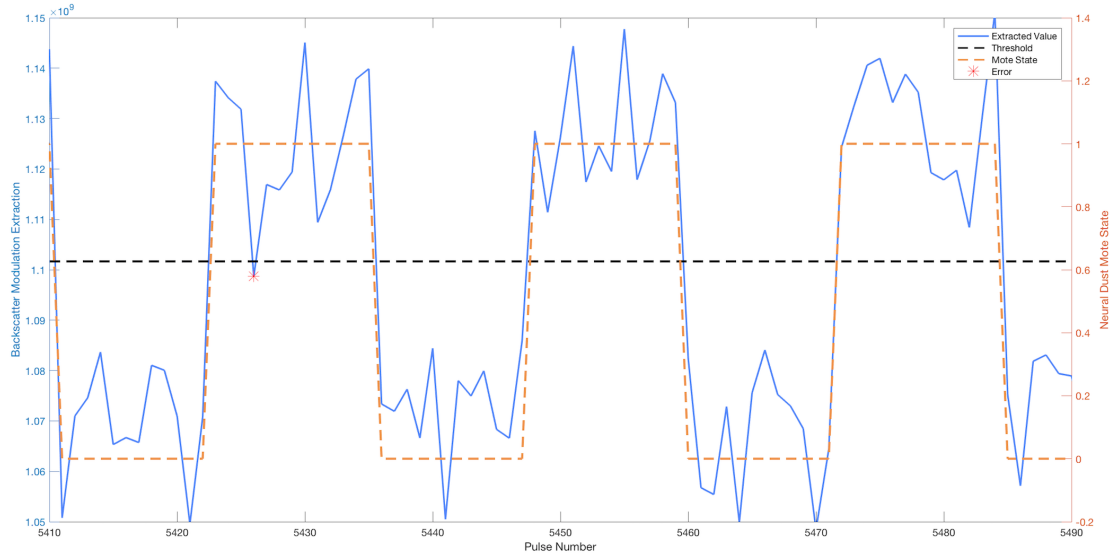


Figure 4.6: Interrogated extracted value error

4.4 Discussion

This work shows that ultrasonic backscatter interrogation is applicable for real-time communication between an implantable sensor and remote client using a rodent-wearable device. A generic digital encoding scheme implemented by controlling the impedance across the dust mote's piezoelectric crystal demonstrates robustness with

a large noise margin. Wirelessly transmitting the extracted backscatter value of the dust mote modulated by “hello world” illustrates the device’s real time communication link with implanted devices. The system’s resiliency to noise depends heavily on the modulation depth of the backscatter signals, which is found to be 6.45%. The effectiveness of the wireless link is emphasized by the system’s low BER of 0.16%. Modulation depth variance is expected in the *in-vivo* environment as interrogation distance and mote orientation changes with the subject’s movements. Frequent threshold calibration may be mandatory to compensate for slight shifts in dust mote position and orientation. Additionally, beamforming techniques may be implemented to track dust mote movement over time for the best signal to noise ratio. Despite these challenges, the robustness of the wearable system’s real-time modulation extraction for digital encoding highlights ultrasonic backscatter interrogation as a promising communication link between implantable sensors and external devices.

Chapter 5

Conclusion

5.1 Future Work

The system's adaptable design creates opportunities to evolve with implantable sensor developments. Moreover, flexible signal processing capabilities allow for progress in implantable sensor interfacing and neural feature extraction. For instance, beam-forming techniques are being explored for simultaneous interrogation of multiple implantable sensors. Such a development will allow the device to adaptively extract signals from individual sensor motes without careful alignment or known mote orientation information prior to extraction. Additionally, the real-time wireless communication link established between the external interrogator and the neural dust mote invites developments toward closed-loop neuromodulation systems to connect the brain with external devices. This link provides an entry point to fully realized brain machine interfacing systems utilizing ultrasonic backscatter communication for applications such as neuromuscular restoration.

Further validation is needed to characterize the system's performance involving signals more representative of neural activity. Resolving analog modulated dust motes may prove challenging and ultimately inaccurate during real time operation given backscatter temporal jitter. The digital implantable device paradigm in which implantable devices convert analog neural signals to binary modulation presents a more robust ultrasonic backscatter interrogation model. This sensing modality will require development toward a communication protocol capable of interpreting multiple bits per interrogation as the neural dust technology evolves toward higher resolutions; moreover, advancements in implantable sensor technology and interrogation devices must occur in unison to realize the most effective and efficient communication technique for ultrasonic interrogation of implantable sensors.

5.2 Summary

The wireless ultrasound interrogation device presented marks a necessary step toward the development of practical brain machine interfacing technology. The neural interfacing system addresses three critical problems with current brain machine interfacing technology: portable, convenient signal-acquisition hardware, real-time operation, and long-term experimental validation. The wearable system allows for *in-vivo* rodent experimentation necessary to progress toward human brain machine interfacing. A generic digital encoding scheme intended for transmission of neural data such as digitized extracellular potential recordings or neural spike counts is demonstrated. The system is validated by modulating the implantable sensor mote, extracting the backscatter modulation in real-time, and transmitting that data to a remote client over Bluetooth. This device is intended to enable awake, unconstrained neuromodulation experiments in animal models and works toward a generalizable neural interface.

Acknowledgements

I would like to thank David Piech for his valuable collaboration throughout the design process, especially for his work designing and fabricating the piezoelectric transducer array and neural dust mote. In addition, I would like to thank both Professor Bernhard Boser and Professor Michel Maharbiz for their exceptional insight and extensive technical knowledge that guided me through this research.

Bibliography

- [1] D. Seo, R. M. Neely, K. Shen, U. Singhal, E. Alon, J. M. Rabaey, J. M. Carmena, and M. M. Maharbiz, “Wireless recording in the peripheral nervous system with ultrasonic neural dust,” *Neuron*, vol. 91, no. 3, pp. 529–539, 2016.
- [2] J. Charthad, S. Baltsavias, D. Samanta, T. C. Chang, M. J. Weber, N. Hosseini-Nassab, R. N. Zare, and A. Arbabian, “An ultrasonically powered implantable device for targeted drug delivery,” *IEEE Engineering in Medicine and Biology Society Conference*, 2016.
- [3] J. J. Shih, D. J. Krusienski, and J. R. Wolpaw, “Brain-computer interfaces in medicine,” in *Mayo Clinic Proceedings*, vol. 87. Elsevier, 2012, pp. 268–279.
- [4] R. J. Vetter, J. C. Williams, J. F. Hetke, E. A. Nunamaker, and D. R. Kipke, “Chronic neural recording using silicon-substrate microelectrode arrays implanted in cerebral cortex,” *IEEE transactions on biomedical engineering*, vol. 51, no. 6, pp. 896–904, 2004.
- [5] K. J. Friston, P. Fletcher, O. Josephs, A. Holmes, M. Rugg, and R. Turner, “Event-related fmri: characterizing differential responses,” *Neuroimage*, vol. 7, no. 1, pp. 30–40, 1998.
- [6] E. W. Sellers, T. M. Vaughan, and J. R. Wolpaw, “A brain-computer interface for long-term independent home use,” *Amyotrophic lateral sclerosis*, vol. 11, no. 5, pp. 449–455, 2010.
- [7] J. R. Wolpaw and D. J. McFarland, “Control of a two-dimensional movement signal by a noninvasive brain-computer interface in humans,” *Proceedings of the National Academy of Sciences of the United States of America*, vol. 101, no. 51, pp. 17 849–17 854, 2004.

- [8] C. Neuper, G. R. Müller-Putz, R. Scherer, and G. Pfurtscheller, “Motor imagery and eeg-based control of spelling devices and neuroprostheses,” *Progress in brain research*, vol. 159, pp. 393–409, 2006.
- [9] D. J. McFarland and J. R. Wolpaw, “Brain-computer interface operation of robotic and prosthetic devices,” *Computer*, vol. 41, no. 10, 2008.
- [10] S. P. Kelly, E. C. Lalor, C. Finucane, G. McDarby, and R. B. Reilly, “Visual spatial attention control in an independent brain-computer interface,” *IEEE Transactions on Biomedical Engineering*, vol. 52, no. 9, pp. 1588–1596, 2005.
- [11] S. P. Kelly, E. C. Lalor, R. B. Reilly, and J. J. Foxe, “Visual spatial attention tracking using high-density ssvep data for independent brain-computer communication,” *IEEE Transactions on Neural Systems and Rehabilitation Engineering*, vol. 13, no. 2, pp. 172–178, 2005.
- [12] B. Z. Allison, D. J. McFarland, G. Schalk, S. D. Zheng, M. M. Jackson, and J. R. Wolpaw, “Towards an independent brain-computer interface using steady state visual evoked potentials,” *Clinical neurophysiology*, vol. 119, no. 2, pp. 399–408, 2008.
- [13] L. J. Trejo, R. Rosipal, and B. Matthews, “Brain-computer interfaces for 1-d and 2-d cursor control: designs using volitional control of the eeg spectrum or steady-state visual evoked potentials,” *IEEE transactions on neural systems and rehabilitation engineering*, vol. 14, no. 2, pp. 225–229, 2006.
- [14] J. R. Manning, J. Jacobs, I. Fried, and M. J. Kahana, “Broadband shifts in local field potential power spectra are correlated with single-neuron spiking in humans,” *Journal of Neuroscience*, vol. 29, no. 43, pp. 13 613–13 620, 2009.
- [15] J. Niessing, B. Ebisch, K. E. Schmidt, M. Niessing, W. Singer, and R. A. Galuske, “Hemodynamic signals correlate tightly with synchronized gamma oscillations,” *science*, vol. 309, no. 5736, pp. 948–951, 2005.
- [16] R. Scherer, S. P. Zanos, K. J. Miller, R. P. Rao, and J. G. Ojemann, “Classification of contralateral and ipsilateral finger movements for electrocorticographic brain-computer interfaces,” *Neurosurgical Focus*, vol. 27, no. 1, p. E12, 2009.
- [17] A. Gunduz, J. C. Sanchez, P. R. Carney, and J. C. Principe, “Mapping broadband electrocorticographic recordings to two-dimensional hand trajectories in humans: motor control features,” *Neural Networks*, vol. 22, no. 9, pp. 1257–1270, 2009.

- [18] G. Schalk, J. Kubanek, K. Miller, N. Anderson, E. Leuthardt, J. Ojemann, D. Limbrick, D. Moran, L. Gerhardt, and J. Wolpaw, "Decoding two-dimensional movement trajectories using electrocorticographic signals in humans," *Journal of neural engineering*, vol. 4, no. 3, p. 264, 2007.
- [19] P. R. Kennedy and R. A. Bakay, "Restoration of neural output from a paralyzed patient by a direct brain connection," *Neuroreport*, vol. 9, no. 8, pp. 1707–1711, 1998.
- [20] J. C. Barrese, N. Rao, K. Paroo, C. Triebwasser, C. Vargas-Irwin, L. Franquemont, and J. P. Donoghue, "Failure mode analysis of silicon-based intracortical microelectrode arrays in non-human primates," *Journal of neural engineering*, vol. 10, no. 6, p. 066014, 2013.
- [21] R. Muller, H.-P. Le, W. Li, P. Ledochowitsch, S. Gambini, T. Bjorninen, A. Koralek, J. M. Carmena, M. M. Maharbiz, E. Alon *et al.*, "A minimally invasive 64-channel wireless μ ecog implant," *IEEE Journal of Solid-State Circuits*, vol. 50, no. 1, pp. 344–359, 2015.
- [22] J. M. Rabaey, M. Mark, D. Chen, C. Sutardja, C. Tang, S. Gowda, M. Wagner, and D. Werthimer, "Powering and communicating with mm-size implants," in *2011 Design, Automation Test in Europe*, March 2011, pp. 1–6.
- [23] D. Seo, J. M. Carmena, J. M. Rabaey, E. Alon, and M. M. Maharbiz, "Neural dust: An ultrasonic, low power solution for chronic brain machine interfaces," *arXiv:1307.2196 [q-bio.NC]*, 2013.
- [24] D. Seo, J. M. Carmena, J. M. Rabaey, M. M. Maharbiz, and E. Alon, "Model validation of untethered, ultrasonic neural dust motes for cortical recording," *Journal of neuroscience methods*, vol. 244, pp. 114–122, 2014.
- [25] D. Seo, H.-Y. Tang, J. M. Carmena, J. M. Rabaey, E. Alon, B. E. Boser, and M. M. Maharbiz, "Ultrasonic beamforming system for interrogating multiple implantable sensors," *IEEE Engineering in Medicine and Biology Society Conference*, 2015.
- [26] D. Dardari and R. D'Errico, "Passive ultrawide bandwidth rfid," *IEEE GLOBE-COM*, 2008.
- [27] F. Mazzilli, M. Peisino, R. Mitouassiyou, B. Cotté, P. Thoppay, C. Lafo, P. Favre, E. Meurville, and C. Dehollain, "In-vitro platform to study ultrasound

- as source for wireless energy transfer and communication for implanted medical devices,” *IEEE Engineering in Medicine and Biology Society Conference*, 2010.
- [28] S. Ozeri and D. Shmilovitz, “Simultaneous backward data transmission and power harvesting in an ultrasonic transcutaneous energy transfer link employing acoustically dependent electric impedance modulation,” *Ultrasonics*, 2014.
 - [29] K. Chatar and M. L. George, “Analysis of existing designs for fpga-based ultrasound imaging systems,” *International Journal of Signal Processing, Image Processing and Pattern Recognition*, vol. 9, no. 7, pp. 13–24, 2016.
 - [30] G.-D. Kim, C. Yoon, S.-B. Kye, Y. Lee, J. Kang, Y. Yoo, and T.-K. Song, “A single fpga-based portable ultrasound imaging system for point-of-care applications,” *IEEE transactions on ultrasonics, ferroelectrics, and frequency control*, vol. 59, no. 7, 2012.
 - [31] C.-K. Weng, J.-W. Chen, and C.-C. Huang, “A fpga-based wearable ultrasound device for monitoring obstructive sleep apnea syndrome,” in *Ultrasonics Symposium (IUS), 2015 IEEE International*. IEEE, 2015, pp. 1–4.
 - [32] P.-W. Cheng, C.-C. Shen, and P.-C. Li, “Mpeg compression of ultrasound rf channel data for a real-time software-based imaging system,” *IEEE transactions on ultrasonics, ferroelectrics, and frequency control*, vol. 59, no. 7, 2012.
 - [33] T. Suenaga, H. Sasaki, Y. Masuda, M. Imura, Y. Yasumuro, A. Yutani, Y. Manabe, O. Oshiro, and K. Chihara, “Wearable ultrasound device for ubiquitous medical care environments,” in *International Congress Series*, vol. 1268. Elsevier, 2004, pp. 265–270.
 - [34] H.-Y. Tang, Y. Lu, X. Jiang, E. J. Ng, J. M. Tsai, D. A. Horsley, and B. E. Boser, “3-d ultrasonic fingerprint sensor-on-a-chip,” *IEEE Journal of Solid-State Circuits*, vol. 51, no. 11, pp. 2522–2533, 2016.
 - [35] H.-Y. Tang, D. Seo, U. Singhal, X. Li, M. M. Maharbiz, E. Alon, and B. E. Boser, “Miniaturizing ultrasonic system for portable health care and fitness,” *IEEE transactions on biomedical circuits and systems*, vol. 9, no. 6, pp. 767–776, 2015.
 - [36] T. L. Szabo, *Diagnostic ultrasound imaging: inside out*. Academic Press, 2004.

- [37] R. Krimholtz, D. A. Leedom, and G. L. Matthaei, "New equivalent circuits for elementary piezoelectric transducers," *Electronics Letters*, vol. 6, no. 13, pp. 398–399, 1970.
- [38] D. M. Pozar, *Microwave engineering*. John Wiley & Sons, 2009.
- [39] E. Ades, "Species specific information: Rat," 2016. [Online]. Available: Web.jhu.edu
- [40] H.-Y. Tang, Y. Lu, S. Fung, D. A. Horsley, and B. E. Boser, "11.8 integrated ultrasonic system for measuring body-fat composition," in *Solid-State Circuits Conference-(ISSCC), 2015 IEEE International*. IEEE, 2015, pp. 1–3.
- [41] L. W. Ritchey, J. Zasio, and K. J. Knack, *Right the first time*. Speeding Edge, 2006.
- [42] J. Carlsson, "Crosstalk on printed circuit boards," *SP Rapport*, p. 14, 1994.
- [43] R. E. Davidsen and S. W. Smith, "Two-dimensional arrays for medical ultrasound using multilayer flexible circuit interconnection," *IEEE Transactions on Ultrasonics, Ferroelectrics, and Frequency Control*, vol. 45, no. 2, pp. 338–348, 1998.
- [44] J. Strole, S. Corbett, W. Lee, E. Light, and S. Smith, "A novel flex circuit area-array interconnect system for a catheter-based ultrasound transducer," *IMAPS 2002*, pp. 338–348, 2002.
- [45] M. Rao, T. Varghese, and J. A. Zagzebski, "Simulation of ultrasound two-dimensional array transducers using a frequency domain model," *Med. Phys.*, vol. 35, no. 7, pp. 3162–3169, 2008.
- [46] Y. Li and J. A. Zagzebski, "A frequency domain model for generating b-mode images with array transducers," *IEEE Transactions on Ultrasonics, Ferroelectrics, and Frequency Control*, vol. 46, no. 3, pp. 690–699, 1999.
- [47] H. Wang, T. Ritter, W. Cao, and K. Shung, "High frequency properties of passive materials for ultrasonic transducers," *IEEE Transactions on Ultrasonics, Ferroelectrics, and Frequency Control*, vol. 48, no. 1, pp. 78–84, 2001.